Performance of ZnFe$_2$O$_4$ as a photoabsorber in solution-processed all-oxide planar photovoltaics

Parul Garg,[1] Sanchari Bhattacharya ,[2] Arpita Paul,[1] Sanjoy Datta,[2] and Ashok Bera [1,*]

[1]*Department of Physics, Indian Institute of Technology Jammu, Jammu and Kashmir 181221, India*
[2]*Department of Physics and Astronomy, National Institute of Technology Rourkela, Odisha 769008, India*

Low-cost, stable, environment-friendly solar cells are the key aspects of modern-day photovoltaics, and oxide absorbers have become the focus of work towards stable devices. Here we explore the viability of semiconducting transition-metal spinel oxide ZnFe$_2$O$_4$ (ZFO) as an absorber layer in solution-processed all-oxide planar solar cells. A 300 nm thick spin-coated ZFO shows a typical cubic spinel structure with a calculated band gap of 1.68 eV, as estimated from density functional theory. Absorption and emission spectra show a direct band gap of 2.19 eV with a maximum absorption coefficient of 10^5/cm, and the film shows a steady increase in photocurrent on illumination by white light. A conventional solution-grown TiO$_2$/ZFO/NiO all-oxide thin film heterojunction solar cell prepared on the fluorine-doped tin oxide coated glass substrate shows an open circuit voltage (V_{OC}) of 519 mV under air mass 1.5 solar illumination. Furthermore, upon doping the TiO$_2$ layer with lithium, enhancement in recombination resistance and reduction of charge transfer resistance results in an increased V_{OC} of 640 mV. Our result introduces spinel oxide as a stable alternative for a photoabsorber in all-oxide photovoltaics, enhancing the multifunctionality of spinel ferrites.

I. INTRODUCTION

Over the last decade, metal oxide semiconductors have been considered integral to modern-day cost-effective solar cells [1–4]. Although oxides like TiO$_2$ [5], ZnO [6], SnO$_2$ [7], Zn$_2$SnO$_4$, [8], SrTiO$_3$, [9], and Nb$_2$O$_5$ [10] have been employed as efficient electron transporting layers (ETLs), in some cases, NiO [11], V$_2$O$_5$ [12], and MoO$_3$ [13] have been used as hole-transporting layers (HTLs). The wide-band-gap nature of all these oxides limits their application as the photoabsorber layer, and materials like organic or hybrid perovskites have gained preference as the absorber layers in thin film solar cells [14,15]. However, the lack of environmental stability of efficient organic or hybrid absorber materials has encouraged researchers to look for metal oxides as a stable alternative absorber material. In this regard, transition-metal spinel oxides with structural formula MFe$_2$O$_4$ (M: Cu, Zn, Ca, Mn, Co, etc.) having direct band gap (E_g) around 2 eV are considered promising materials for utilization as photoabsorbers in optoelectronic devices [16,17]. These metal oxides find extensive utility across various domains, such as sensors [18], resistive switching [19], photoelectrochemical water splitting [20], photocatalysis [21], photodetectors [22], Li-ion batteries [23], and more [24]. Among these spinel oxides, ZnFe$_2$O$_4$ (ZFO) is a multifunctional material specially featured as a ferrimagnetic oxide [25–29]. With a high Earth abundance of Zn and Fe [30], ZFO is a low-cost, nontoxic material with a direct E_g of 1.6–2.3 eV and a high absorption coefficient [30–35]. Although ZFO exhibits this substantial

potential, it has seldom been studied as a potential solar-absorber material in photovoltaics.

The present work explores the feasibility of solution-processed ZFO thin film as a photoabsorber layer in solar cells and studies its photovoltaic performance. A spin-coated ZFO thin film on a fluorine-doped tin oxide (FTO) coated glass substrate shows a single-phase spinel cubic crystal structure, and the density functional theory calculation shows an electrical E_g of around 1.68 eV. However, the absorption and emission spectra reveal a direct E_g of the order of 2.19 eV with an absorption coefficient as high as 10^5/cm. A steady rise under illumination in the transient photocurrent response of the ZFO films confirms its visible light sensitivity. The solution-processed all-oxide TiO$_2$/ZFO/NiO-based heterojunction shows typical diode like current-voltage (I-V) characteristics, which exhibit a photovoltage of 519 mV under the standard air mass (AM) 1.5 (100 mW cm^{-2}) irradiation, showing the photovoltaic capability of ZFO. Further, doping 5% lithium (Li) in TiO$_2$ increased the V_{OC} to 640 mV for Li-TiO$_2$/ZFO/NiO all-oxide solar cells. Being all-oxide solar cells, these devices show no significant changes in the photovoltaic performance even after a month of storage in environmental conditions or annealing at 80°C after dropwise water addition. The results here introduce ZFO as a stable, low-cost absorber in all-oxide photovoltaics that further enhances the multifunctionality of spinel ferrites.

II. EXPERIMENTAL SECTION

Following the previous report, the ZFO thin films were prepared using the solution-processed spin-coating method [36]. In brief, the precursor solution was prepared using Zn(NO$_3$)$_2$ · 6H$_2$O and Fe(NO$_3$)$_3$ · 9H$_2$O as starting

*ashok.bera@iitjammu.ac.in

materials and 2-methoxy ethanol as solvent. $Zn(NO_3)_2 \cdot 6H_2O$ and $Fe(NO_3)_3 \cdot 9H_2O$ were added in the molar ratio of 1:2 in the solvent to obtain a 0.2 M solution, and the mixture was stirred at room temperature for 3 h. The solution was stable for more than 1 month at room temperature. ZFO thin films were deposited on quartz and FTO substrates by spin-coating the above-prepared precursor solution at a rotating speed of 2000 rpm for 30 s and then annealing at 300°C for 15 min on a hot plate. Similar deposition procedures were repeated to achieve the desired film thickness. The yellowish-orange-colored thin films were finally annealed at 500°C for 1 h in the muffle furnace for final crystallization.

The solar cells were fabricated on FTO-coated glass substrates by spin coating following our previous report [37]. The FTO substrates (size: 20 mm × 20 mm and sheet resistance: 20 $\Omega/\square$) were washed with 2% Hellmanex solution, distilled water, acetone, and methanol for 10 min each in a sonicator. Before deposition of ZFO, compact TiO_2 and Li-doped TiO_2 as the ETL were spin-coated onto the FTO substrate from a mixture solution of 370 µl of titanium isopropoxide, and 5 ml of ethanol and 35 µl of HCl at 2000 rpm for 30 s, and then dried at 200°C for 10 min on a hot plate, followed by annealing at 500°C for 30 min in a muffle furnace. Li doping of TiO_2 was accomplished by doping 5% bis(trifluoromethane) sulfonimide lithium salt (LiTFSI, 99.95%, Aldrich) in a TiO_2 precursor solution. ZFO thin film layers with thicknesses around 300 nm were deposited on TiO_2 to prepare a heterojunction, followed by deposition of p-type NiO thin film. To prepare the NiO precursor solution, 0.25 M nickel acetate dihydrate was dissolved in isopropyl alcohol, and the resultant mixture was stirred continuously for 3 h until a homogeneous solution with a light green color was obtained. This solution was then spin coated and subsequently annealed at 500°C for 30 min to obtain the polycrystalline NiO thin film. Finally, the top contact was made by depositing an 80 nm Au electrode using the thermal evaporation technique, and the total device area was 0.0314 cm^2.

To determine the crystalline phase of the fabricated ZFO thin films, x-ray diffraction (XRD) analysis was done using Cu $K\alpha$ radiation, $\lambda = 1.5406$ Å (Panalytical Empyrean), and the data were analyzed with X'Pert High Score software. The Raman spectrum was measured using a laser Raman spectrophotometer (WITec alpha300) with a CCD camera using an Ar ion laser (532 nm) over 200-800 cm^{-1}. The surface morphologies of the ZFO thin films were examined by a field emission scanning electron microscope (FESEM) (model: JEOL JSM-7900F) and an atomic force microscope (AFM) (Cypher S AFM, Asylum Research). Quantitative x-ray photoelectron spectroscopy (XPS) (Model: Nexsa, ThermoFisher) studies were performed to govern the chemical composition and the valence state of the elements present in the sample using Al $K\alpha$ radiation (1486.6 eV). The spot size of the irradiated area was 400 µm, and the base pressure of the analysis chamber was in the range of 10^{-8} Pa. All the binding energies in the XPS spectra were corrected for specimen charging by reflecting them to the C 1s peak at 284.8 eV. The absorption spectrum of the ZFO film was acquired by a UV-VIS spectrophotometer (Cary 5000). The photoluminescence (PL) spectrum was recorded by exciting the ZFO film with a He-Cd laser (wavelength 325 nm, Kimmon Koha

Co. Ltd.; model KR1801C), and the emission spectrum was recorded using a high-resolution spectrometer (Horiba Jobin Yvon model iHR 320). The two-probe method was used to study the electrical resistivity (ρ) of the ZFO thin films in the temperature range 298–523 K, where the temperature was varied with a proportional integral differential (PID) operating controller. The resistance value of the solution-processed ZFO films was much higher at lower temperatures, limiting the measurement capabilities below 298 K. Ultraviolet photoelectron spectroscopy (UPS) measurements were performed using He (I) ($E_{max} = 21.22$ eV) source (Nexsa, ThermoFisher) to estimate the work function value of TiO_2, Li-TiO_2, and ZFO thin films. The photovoltaic measurements were carried out under the illumination of 100 mW cm^{-2}, generated by a AAA solar simulator (Abet 11000A). I-V characteristics were measured under dark and 1 Sun (AM 1.5) illumination with the Keithley 2450 source meter unit. Electrochemical impedance spectroscopy (EIS) measurements were performed using an electrochemical workstation (CHI 1150C, CH Instruments), where a small ac perturbation of 500 mV was applied to the devices, and the different impedance output was measured throughout a frequency range of 1 MHz–1 Hz.

III. RESULTS AND DISCUSSION

The XRD spectrum [Fig. 1(a)] of the spin-coated ZFO film on a FTO substrate shows diffraction peaks at 2θ values 30.18°, 35.60°, 43.11°, 53.40°, 57.00°, and 62.45°, which can be indexed to the crystal planes (220), (311), (400), (422), (511), and (440), respectively (Crystallography Open Database Ref. No. 01-089-1009). Figure 1(b) shows the corresponding atomic arrangements of ZFO in a typical cubic crystal structure within the face-centered cubic arrangement of the oxygen anions. It exhibits the normal spinel structure in which the octahedrally coordinated B sites are solely populated with the Fe^{3+} cations, whereas the tetrahedrally coordinated A sites accommodate divalent Zn^{2+} cations [38]. Figure S1 in the Supplemental Material [39] displays the room temperature Raman spectrum of the ZFO thin film, which shows three characteristic Raman modes corresponding to F_{2g} (2), F_{2g} (3), and A_{1g} symmetries at 332–372, 478–540, and 620-690 cm^{-1}, respectively. The A_{1g} modes with frequencies exceeding 600 cm^{-1} are primarily associated with the movement of oxygen atoms within the tetrahedral AO_4 groups [40]. In contrast, the other low-frequency modes represent the characteristics of the octahedral sites (BO_6) [41]. The surface morphology of the solution-grown thin films was analyzed using FESEM [Fig. 1(c)], which shows perfectly smooth morphology with an interconnected wormlike grain association with an average grain size of ZFO around ~30 nm (as shown by the histogram given in the inset of Fig. 1(c). The surface morphology was further analyzed using AFM [Fig. 1(d)]. The root mean square surface roughness was measured in the range of 1.39–2.136 nm from the corresponding three-dimensional atomic force micrograph, given in Fig. S2 [39], which further reaffirms that the films are flat.

The full scan XPS spectrum of ZFO in Fig. 2(a) shows that Zn, Fe, and O are the main elements of ZFO thin films. The Zn 2p core-level spectrum consists of Zn 2$p_{3/2}$ (1021.55 eV) and Zn 2$p_{1/2}$ (1044.58 eV) peaks [Fig. 2(b)], validating the
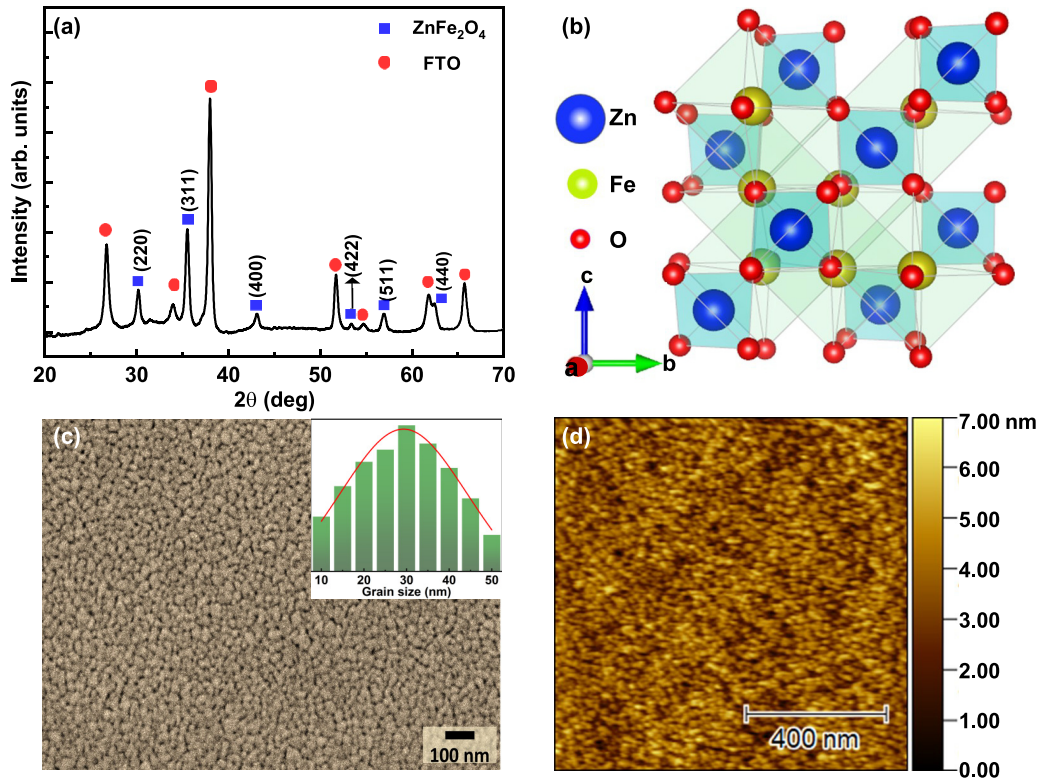
FIG. 1. (a) XRD pattern of the ZFO thin film (blue squares) grown on FTO (red circles) coated glass substrate. (b) Schematic view of the cubic spinel structure of ZFO with octahedral (green) and tetrahedral (blue) units. Oxygen atoms are represented in red at the corners. (c) Top-view FESEM image of ZFO thin film along with grain size distribution curve (inset of this figure) and (d) two-dimensional AFM image of the solution-processed ZFO film on top of the quartz substrate.

occurrence of divalent Zn in the ZFO film [42]. Figure 2(c) shows the Fe $2p$ high-resolution spectrum demonstrating the Fe^{2+} and Fe^{3+} states of Fe $2p_{3/2}$ and Fe $2p_{1/2}$ doublets, along with their satellite peaks. The peaks at around 711 and 724 eV correspond to the Fe^{2+} species (blue), while those around 713 and 727 eV belong to the Fe^{3+} species (pink) [43]. The cation ratio between Zn and Fe in the ZFO film was estimated to be 9.21:20.17, in which the Zn:Fe ratio is slightly lower than the ideal ratio of 1:2 in $ZnFe_2O_4$, showing the presence of Zn ion vacancies in the solution-processed ZFO films. Furthermore, the high-resolution O $1s$ spectrum in Fig. 2(d) presents a broad asymmetric curve deconvoluted into three peaks with binding energies (B.Es) at 532.8, 531.6, and 530.1 eV. Generally, the peak at 530.1 eV is characteristic of surface lattice oxygen, the higher binding energy peak at around 531.6 eV is due to oxygen vacancies in ZFO, and the other peak sitting at 532.8 eV is due to the surface adsorbed oxygen species such as O_{2ads}^- and O_{ads}^- [34].

The optical absorption spectrum of the 300 nm thick ZFO films in the wavelength range of 700–300 nm is depicted in Fig. 3(a), which shows that, although the absorption edge begins nearly at 650 nm, the absorption starts to increase significantly at a value of 530 nm (absorption coefficient over 10^4/cm) with a very sharp absorption at around 450 nm; the absorption coefficient reaches 10^5/cm nearly at 400 nm, making the material well suited for light-harvesting applications. The corresponding optical E_g value was calculated from the Tauc plot drawn between $(\alpha h\nu)^2$ vs $h\nu$ where α is the absorption coefficient corresponding to $h\nu$:, h is Planck's constant,

and ν is the frequency of the incident photon. The Tauc plot in Fig. 3(b) shows two prominent direct optical Eg at 2.19 eV (E_{g1}) and 2.63 eV (E_{g2}). The PL spectrum of the ZFO thin film in Fig. 3(c) shows two major peaks at 434 and 535 nm, confirming the direct E_g nature of the ZFO material.

To substantiate the experimental results for ZFO thin films, its electronic-band structure and density of states (DOS) were computed [Figs. 4(a) and 4(b)] through a first-principles approach within the density functional theory (DFT) framework, employing QUANTUM ESPRESSO software [44]. The crystal structure of ZFO belongs to the C_{2v} point group. In this study, a projected augmented wave (PAW) type basis set [45] was utilized, employing the generalized gradient approximation [46] implemented in the Perdew-Burke-Ernzerhof (PBE) exchange-correlation functionals [47]. The presumed magnetic ground state is characterized by a collinear arrangement of antiferromagnetic order, where the positioning of magnetic spins aims to achieve the lowest possible total energy. The band structure shows an electronic transition with a direct E_g of 1.68 eV, and the absorption mainly arises from O $2p$ to Fe $3d$ interband transitions. Since E_g are underestimated within DFT, it is, therefore, reasonable that experimentally measured absorption peaks are at higher energies [48]. In this study, the spin arrangement is derived from a prior investigation into the magnetic ground state of ZFO [49]. Two distinct spin states are designated as Fe1 and Fe2. To account for the strongly correlated Fe $3d$ and Zn $3d$ states, the PBE+U method is employed [50], with Hubbard U set to 5 eV. Ionic relaxation is achieved with a
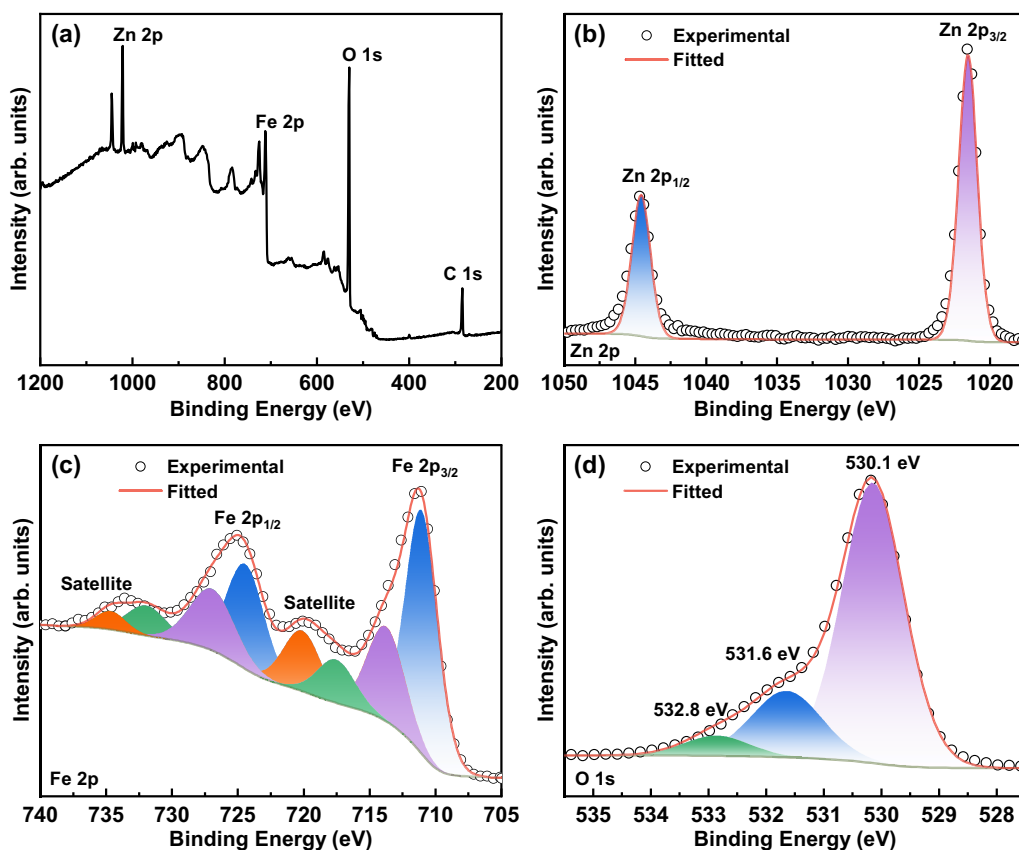
FIG. 2. (a) XPS survey spectrum showing the presence of Zn, Fe, O, and C. High-resolution fitted spectra of (b) Zn $2p$, (c) Fe $2p$, and (d) O $1s$.

convergence threshold for interatomic forces set to less than 10^{-3} Ry/bohr. To ensure the convergence of self-consistent calculations, a cutoff energy of 80 Ry and an automatic $8 \times 8 \times 8$ k−point grid using the Monkhorst-Pack scheme are employed. Gaussian-type broadening with a width of 0.01 Ry is applied in all calculations.

Further, to study the carrier transport mechanism in ZFO, the resistivity vs temperature (ρ-T) curve of the ZFO thin film was measured in the temperature range 298–530 K, and the activation energy (E_a) was estimated using the Arrhenius model, which is described by the equation

$$\rho = \rho_0 \exp\left(\frac{-E_a}{k_B T}\right),$$

where ρ_0 is a constant, and k_B is the Boltzmann constant; the curve plotted between $\ln(\rho)$ and the inverse of the temperature should exhibit linear behavior. As shown in Fig. 4(c), the ρ-T curve of the ZFO film shows a semiconducting behavior in the whole temperature range and the linear fitting of the $\ln \rho$ vs $1000/T$ plot [Fig. 4(d)] shows the active conduction region has an E_a value of 0.28 eV. The calculated value is comparable to one estimated by Rahmouni *et al.* [51]. This linear trend observed in the curve shows that the conduction is associated with structural defects, such as the vacancies and the electron hopping between Fe^{2+} and Fe^{3+} cations distributed randomly through the tetrahedral and octahedral sites in ZFO.

I-V characteristics under dark and light were measured to study the photoresponse of the solution-grown ZFO thin
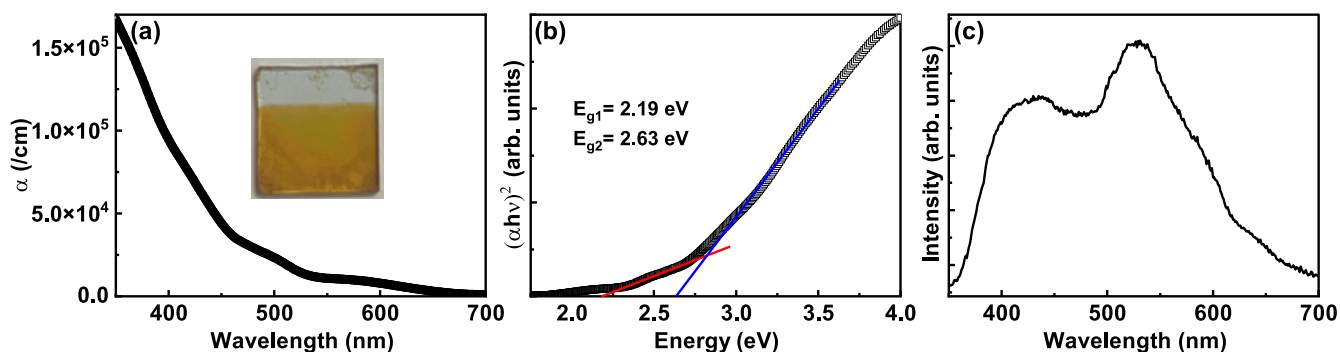

FIG. 3. (a) Optical absorption spectrum, (b) Tauc plot for band gap (E_g) calculation, and (c) PL spectrum of the ZFO thin film.
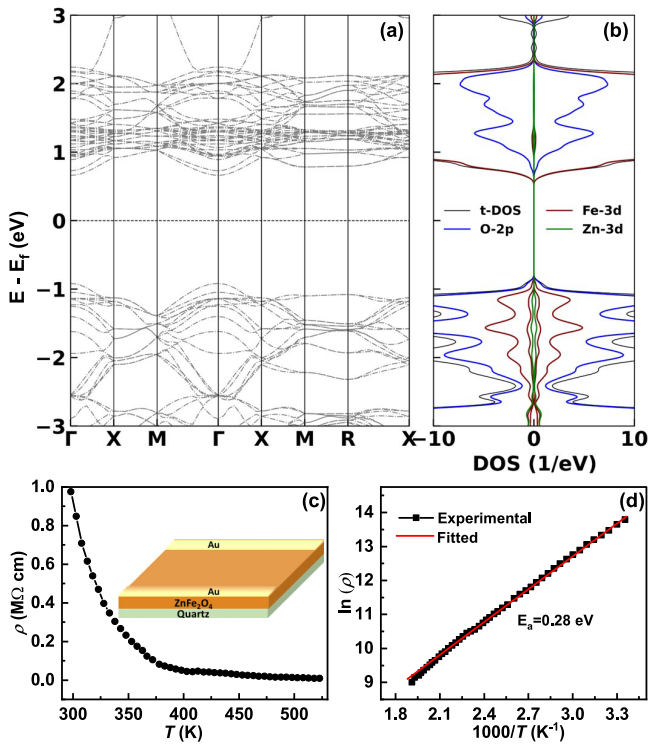
FIG. 4. (a) Electronic band structure of ZFO and (b) electronic density of states (DOS) with partial contributions from O $2p$, Fe $3d$, and Zn $3d$. (c) Resistivity vs temperature (ρ-T) curve measured from the quartz/ZFO film with Au ohmic contact pads. (d) Plot of ln (ρ) as a function of the inverse of temperature.

film. The schematic of the photoresponse measurement on the quartz/ZFO device with interdigitated 80 nm thick Au electrodes on top of ZFO is shown in Fig. 5(a). The *I-V* characteristics of ZFO thin films in Fig. 5(b) show that, on light illumination, the photocurrent increases from 0.12 to 1 μA at a bias of 3 V after 5 min of light illumination. A similar result was also observed in the transient photocurrent-response measurement [Fig. 5(c)], in which the periodic illumination of white light for 2 min, followed by dark for 2 min, provides the repeatable and steady response of the photocurrent, thus validating the light sensitivity of solution-processed ZFO films.
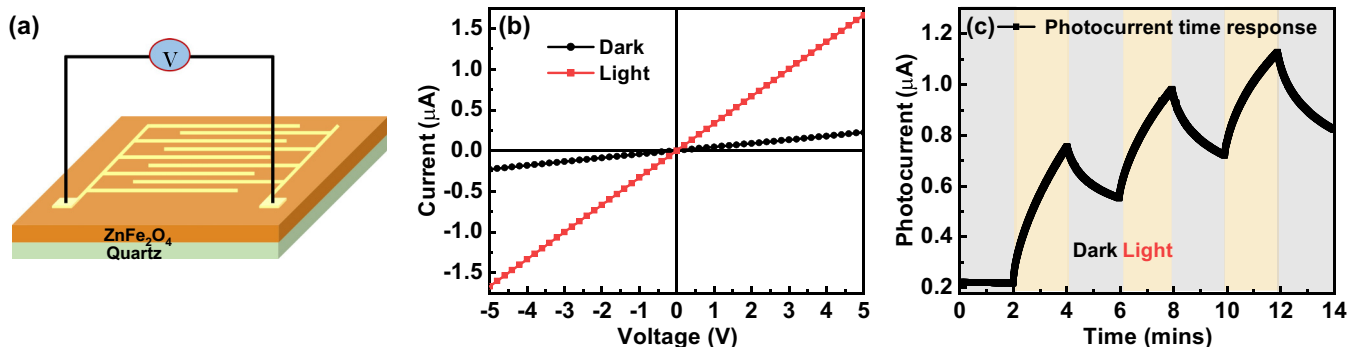
The favorable optical and photoresponse characteristics of solution-processed ZFO thin films encouraged the exploration of their photovoltaic characteristics. We investigated the valence band structure of ZFO films using the UPS technique to establish an appropriate device configuration for a photovoltaic device. As shown in Fig. 6(a), the work function (Φ) was calculated to be ~4.08 eV by subtracting the secondary electron cutoff value of 17.14 eV from the ultraviolet photon energy of 21.22 eV (He I source). The energy difference (E_P) between the valence band maximum (VBM) and the Fermi energy (E_F) is calculated to be 1.80 eV, as inferred from the valence band region in Fig. S3 [39]. Therefore, combining with the above calculated E_g value (from the Tauc plot), VBM and conduction band minimum (CBM) values of ZFO are estimated to be ~−5.9 and −3.7 eV, respectively. Based on this result, the schematic energy band diagram of ZFO with the conventional oxide-based ETL and HTL, i.e., TiO$_2$ and NiO, was constructed, where the VBM and CBM for NiO were taken from the literature [52]. The VBM values of ETLs and the corresponding Fermi levels were measured from the UPS spectra (shown in Fig. S4 [39]). These VBM values were combined with their E_g values (as measured from the Tauc plot and the absorption curves given in Fig. S5 [39]) to determine the CBM values. The estimated band alignments of TiO$_2$ and Li-TiO$_2$ are similar to the previous report by Wang *et al.* [53]. As shown in Fig. 6(b), the band position of ZFO is suitable for directional charge transfer with the ETL and HTL, which is essential for a photovoltaic device. Figure 6(c) illustrates the current density-voltage (*J-V*) characteristics of the TiO$_2$/ZFO/NiO heterojunction device under dark conditions, and the inset shows the cross-sectional FESEM image revealing a layered structure with a 300 nm ZFO layer deposited on top of 100 nm TiO$_2$ layer and 60 nm NiO HTL. Their corresponding elemental mapping was done using energy dispersive x-ray (EDX) analysis. The homogeneous distribution of Ti, Zn, Fe, Ni, and Au in Figure S6 [39] confirms the layered TiO$_2$/ZFO/NiO heterostructure. On illumination from a solar simulator (AM 1.5), the solution-processed TiO$_2$/ZFO/NiO device displayed an average V_{OC} of over 0.5 V, as shown in Fig. 6(d) and Fig. S7 [39] shows very negligible V_{OC} (0.08 V) in only TiO$_2$/NiO devices, showing the photovoltaic performance of the ZFO layer. However, very small grain size and the presence of ionized defects of

FIG. 5. (a) Three-dimensional schematic of the photoresponse measurement setup of solution-processed ZFO on the quartz substrate. (b) *I-V* characteristics of ZFO thin films measured under dark and light conditions. (c) The transient photocurrent response of ZFO film measured under a bias voltage of 3 V.
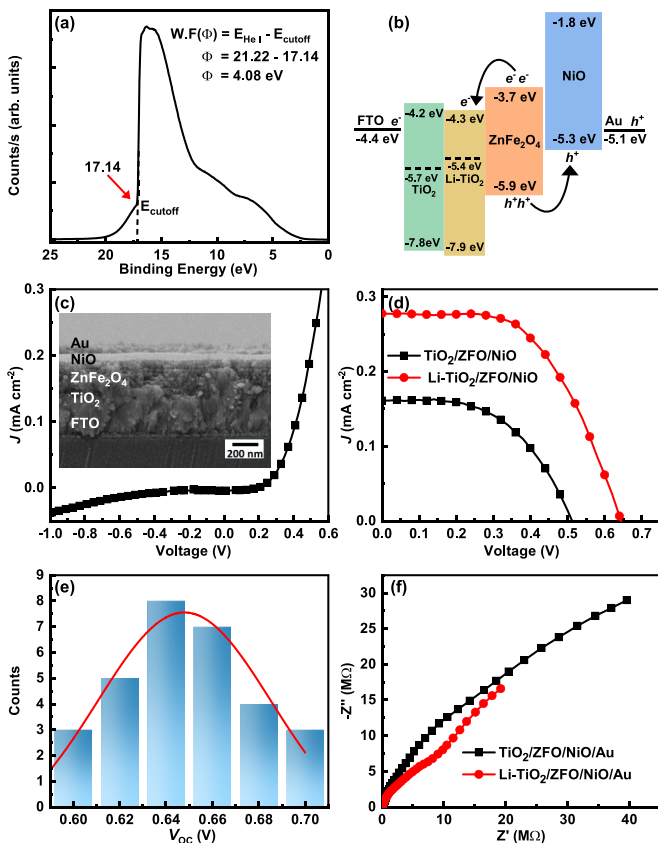
FIG. 6. (a) UPS spectrum of ZFO using He I incident energy source. (b) Schematic energy band diagram of the FTO/Li−TiO$_2$(TiO$_2$)/ZFO/NiO/Au heterojunction. (c) Dark J-V curve with inset showing cross-sectional FESEM image of the ZFO-based heterojunction solar cell. (d) J-V characteristics of ZFO-based solar cells with and without Li metal doping in TiO$_2$ ETL under 1 Sun illumination. (e) Histogram for V_{OC} of 30 solar cells with Li-TiO$_2$ ETL. (f) Nyquist plots of FTO/TiO$_2$/ZFO/NiO/Au and FTO/Li−TiO$_2$/ZFO/NiO/Au heterojunction devices.

the solution-grown ZFO thin film, as observed from FESEM and XPS studies, respectively, give rise to a large number of trapping and recombination centers for the photogenerated carriers, resulting in a low short-circuit current density (J_{SC}) of 0.165 mA cm^{-2} and fill factor (FF) of 48%, and the overall photovoltaic parameters are similar to the previously reported all-oxide solar cells [2,54–56].

To improve the photovoltaic performance of our device, Li was doped to the TiO$_2$ layer, and the Li-TiO$_2$/ZFO/NiO device shows better performance, as plotted in Fig. 6(d) (red line), with the average V_{OC} reaching a value of 0.64 V and a maximum value of about 0.70 V as shown in the histogram plot of the V_{OC} for 30 solar cells [Fig. 6(e)]. The J_{SC} and the FF of the Li-doped devices also increased to 0.277 mA cm^{-2} and 55%, resulting in an average efficiency of 0.1%. It is reported that the presence of oxygen vacancies in the TiO$_2$ lattice leads to the formation of dangling bonds, which easily trap electrons when the electrons are transported from the absorber layer to TiO$_2$. The Li doping helps to passivate the density of electron traps within the TiO$_2$ lattice [57,58]. Li doping usually increases the carrier concen-

tration in TiO$_2$ [59], which may increase the depletion region within ZFO at the TiO$_2$/ZFO interface, which helps in easy charge transfer. To prove our proposition, we performed the electrochemical impedance analysis of the two devices, and the corresponding Nyquist plots of FTO/TiO$_2$/ZFO/NiO/Au and FTO/Li−TiO$_2$/ZFO/NiO/Au are plotted in Fig. 6(f). The semicircle in the high-frequency region is usually regarded as the characteristic of the charge transfer process; at the same time, the linear line at low frequency is attributed to the recombination in the interfaces between different layers. The FTO/Li−TiO$_2$/ZFO/NiO/Au heterojunction has a much smaller arc diameter than FTO/TiO$_2$/ZFO/NiO/Au, indicating that doping Li metal to n-type TiO$_2$ reduces the charge transfer resistance. Therefore, the higher photovoltaic performance after Li doping is attributed to the effective charge separation. Furthermore, Li-doped E_F of TiO$_2$ shifted closer to the conduction band of ZFO [Fig. 6(b)], which also helped to improve the V_{OC}. Another important factor for cost-efficient photovoltaic cells is their durability and stability under harsh environmental conditions. Since our device is all oxide, we added water onto it dropwise (video added in the Supplemental Material [39]) and dried it at 80°C. The device showed only a slight variation in the V_{OC}, as plotted in Fig. S8 [39]. All the devices were also tested after 1 month of storage at environmental conditions to study the durability, and no significant changes in the device performance were observed (Fig. S9 [39]). Although the spinel ferrite ZFO-based device shows stable performance, the efficiency is very low, mainly due to the small grain size of the solution-processed ZFO films. The vapor deposition technique can be utilized to improve the film quality and, hence, to improve the solar cell performance so that ZFO-based devices can be used as semitransparent solar cells or back-gated cells in tandem solar cells.

IV. CONCLUSION

Our work is an attempt to utilize cubic spinel-structured ZFO thin films as an active absorber material in photovoltaic devices. We systematically explored the charge transport and optoelectronic properties of solution-processed ZFO thin films. Although ZFO exhibits a theoretical band gap of 1.68 eV, optical characterization reveals a direct band gap of ∼2.19 eV. An open-circuit voltage of 519 mV was observed in a conventional solution-grown TiO$_2$/ZFO/NiO all-oxide thin film heterojunction solar cell grown on FTO-coated glass substrate under AM 1.5 solar illumination, showing that ZFO possesses potential for being an effective photoabsorber material. Further, we demonstrated that Li doping to TiO$_2$ effectively improved the charge carrier transport and enhanced the electron-hole pair extraction, leading to better photovoltaic performance of Li-TiO$_2$/ZFO/NiO devices with the highest V_{OC} reaching 0.7 V. Further optimization of ZFO based solar cells in terms of film deposition techniques and device design are required to fabricate cost-effective stable semitransparent devices.

[1] E. Assmann, P. Blaha, R. Laskowski, K. Held, S. Okamoto, and G. Sangiovanni, Phys. Rev. Lett. **110**, 078701 (2013).

[2] L. Wang *et al.*, Phys. Rev. Appl. **3**, 064015 (2015).

[3] R. Nechache, C. Harnagea, S. Li, L. Cardenas, W. Huang, J. Chakrabartty, and F. Rosei, Nat. Photonics **9**, 61 (2015).

[4] Z. Fan, K. Yao, and J. Wang, Appl. Phys. Lett. **105**, 162903 (2014).

[5] X. Yin, Z. Xu, Y. Guo, P. Xu, and M. He, ACS Appl. Mater. Interfaces **8**, 29580 (2016).

[6] Z.-L. Tseng, C.-H. Chiang, S.-H. Chang, and C.-G. Wu, Nano Energy **28**, 311 (2016).

[7] A. Akhanuly, I. T. Dossyaev, E. O. Shalenov, C. Valagiannopoulos, K. N. Dzhumagulova, A. Ng, and A. N. Jumabekov, Phys. Rev. Appl. **19**, 054039 (2023).

[8] A. Bera, A. D. Sheikh, M. A. Haque, R. Bose, E. Alarousu, O. F. Mohammed, and T. Wu, ACS Appl. Mater. Interfaces **7**, 28404 (2015).

[9] A. Bera, K. Wu, A. Sheikh, E. Alarousu, O. F. Mohammed, and T. Wu, J. Phys. Chem. C **118**, 28494 (2014).

[10] F. Lenzmann, J. Krueger, S. Burnside, K. Brooks, M. Grätzel, D. Gal, S. Rühle, and D. Cahen, J. Phys. Chem. B **105**, 6347 (2001).

[11] S. Chatterjee, S. K. Saha, and A. J. Pal, Sol. Energy Mater. Sol. Cells **147**, 17 (2016).

[12] S. Ahmmed, A. Aktar, and A. B. M. Ismail, ACS Omega **6**, 12631 (2021).

[13] K. Majhi, L. Bertoluzzi, K. J. Rietwyk, A. Ginsburg, D. A. Keller, and P. Lopez-Varo, Adv. Mater. Interfaces **3**, 1500405 (2016).

[14] S. Wilken, V. Wilkens, D. Scheunemann, R.-E. Nowak, K. von Maydell, J. Parisi, and H. Borchert, ACS Appl. Mater. Interfaces **7**, 287 (2015).

[15] M. Grätzel, Nat. Mater. **13**, 838 (2014).

[16] N. Guijarro, P. Bornoz, M. Prévot, X. Yu, X. Zhu, M. Johnson, X. Jeanbourquin, F. Le Formal, and K. Sivula, Sustain. Energy Fuels **2**, 103 (2018).

[17] K. Dileep, B. Loukya, N. Pachauri, A. Gupta, and R. Datta, J. Appl. Phys. **116**, 103505 (2014).

[18] S. W. Gumbi, P. S. Mkwae, I. Kortidis, R. E. Kroon, H. C. Swart, T. Moyo, and S. S. Nkosi, ACS Appl. Mater. Interfaces **12**, 43231 (2020).

[19] P. Kaith, P. Garg, and A. Bera, Appl. Phys. Lett. **122**, 133301 (2023).

[20] M. Einert *et al.*, Small **19**, 2205412 (2023).

[21] M. P. Dojcinovic, Z. Z. Vasiljevic, V. P. Pavlovic, D. Barisic, D. Pajic, N. B. Tadic, and M. V. Nikolic, J. Alloys Compd. **855**, 157429 (2021).

[22] P.-H. Chung, C.-T. Kuo, T.-H. Wang, Y.-Y. Lu, C.-I. Liu, and T.-R. Yew, ACS Appl. Mater. Interfaces **13**, 6411 (2021).

[23] S. Bourrioux *et al.*, New J. Chem. **41**, 9236 (2017).

[24] D. H. K. Reddy and Y.-S. Yun, Coord. Chem. Rev. **315**, 90 (2016).

[25] V. Zviagin, Y. Kumar, I. Lorite, P. Esquinazi, M. Grundmann, and R. Schmidt-Grund, Appl. Phys. Lett. **108**, 4 (2016).

[26] E. Lišková-Jakubisová, Š. Višňovský, P. Široký, D. Hrabovský, J. Pištora, S. C. Sahoo, S. Prasad, N. Venkataramani, M. Bohra, and R. Krishnan, J. Appl. Phys. **117**, 17B726 (2015).

[27] S. Nakashima, K. Fujita, K. Tanaka, K. Hirao, T. Yamamoto, and I. Tanaka, Phys. Rev. B **75**, 174443 (2007).

[28] M. Bohra, V. Alman, and R. Arras, Nanomaterials **11**, 1286 (2021).

[29] A. Adiba, V. Pandey, T. Ahmad, P. Nehla, and S. Munjal, Phys. B (Amsterdam) **654**, 414742 (2023).

[30] J. H. Kim, H. E. Kim, J. H. Kim, and J. S. Lee, J. Mater. Chem. A **8**, 9447 (2020).

[31] S. Hussain, S. Hussain, A. Waleed, M. M. Tavakoli, S. Yang, M. K. Rauf, Z. Fan, and M. A. Nadeem, J. Phys. Chem. C **121**, 18360 (2017).

[32] J. Ye, S.-Q. Liu, W.-X. Liu, Z.-D. Meng, L. Luo, F. Chen, and J. Zhou, ACS Omega **4**, 6411 (2019).

[33] J. Li, X. Li, Z. Yin, X. Wang, H. Ma, and L. Wang, ACS Appl. Mater. Interfaces **11**, 29004 (2019).

[34] D. Peeters *et al.*, ACS Sustain. Chem. Eng. **5**, 2917 (2017).

[35] M. Mohsen Momeni and M. Najafi, Inorg. Chem. Commun. **132**, 108809 (2021).

[36] P. Garg and A. Bera, Appl. Phys. Lett. **123**, 023301 (2023).

[37] P. Garg, S. Bhattacharya, S. Singla, P. Kaith, S. Datta, B. Chakraborty, and A. Bera, Phys. Rev. Mater. **6**, 085402 (2022).

[38] J. Lumetzberger, V. Ney, A. Zakharova, N. Daffe, D. Primetzhofer, F. Wilhelm, A. Rogalev, and A. Ney, Phys. Rev. B **107**, 144416 (2023).

[39] See Supplemental Material at http://link.aps.org/supplemental/10.1103/PhysRevMaterials.8.065402 for Raman spectrum, Three-dimensional AFM image, Valence band region of UPS spectrum of ZFO film, UPS spectrum and valence band region of TiO$_2$ and Li-TiO$_2$ thin film, Absorption spectra and Tauc plot curves of TiO$_2$ and Li-TiO$_2$ thin films. Cross-sectional EDX images, *J-V* characteristics of TiO$_2$/NiO heterojunction, *J-V* curve of Li-TiO$_2$/ZFO/NiO heterojunction device tested after heating at 80 °C, *J-V* curve of our best-performing Li-TiO$_2$/ZFO/NiO heterojunction device tested after 1 month.

[40] B. Sen Yadav, A. K. Vishwakarma, A. K. Singh, and N. Kumar, Vacuum **207**, 111617 (2023).

[41] S. Restelli, B. Albini, S. Bonomi, M. Bini, M. C. Mozzati, and P. Galinetto, Mater. Today Commun. **35**, 106405 (2023).

[42] A. K. Singh, S. Kumar, B. Sen Yadav, A. K. Vishwakarma, and N. Kumar, Appl. Phys. Lett. **123**, 033902 (2023).

[43] J. G. Monsalve, C. Ostos, E. Ramos, J. G. Ramírez, and O. Arnache, Curr. Appl. Phys. **22**, 77 (2021).

[44] P. Giannozzi *et al.*, J. Phys.: Condens. Matter **21**, 395502 (2009).

[45] P. E. Blöchl, Phys. Rev. B **50**, 17953 (1994).

[46] A. Dal Corso, A. Pasquarello, A. Baldereschi, and R. Car, Phys. Rev. B **53**, 1180 (1996).

[47] J. P. Perdew, K. Burke, and M. Ernzerhof, Phys. Rev. Lett. **77**, 3865 (1996).

[48] J. P. Perdew, Int. J. Quantum Chem. **28**, 497 (2009).

[49] J. J. Melo Quintero, C. E. Rodríguez Torres, and L. A. Errico, J. Alloys Compd. **741**, 746 (2018).

[50] V. I. Anisimov, J. Zaanen, and O. K. Andersen, Phys. Rev. B **44**, 943 (1991).

[51] H. Rahmouni, A. Benali, B. Cherif, E. Dhahri, M. Boukhobza, K. Khirouni, and M. Sajieddine, Phys. B (Amsterdam) **466**, 31 (2015).

[52] Q. Fatima, A. A. Haidry, R. Hussain, and H. Zhang, Energy Fuels **37**, 7411 (2023).

[53] J. Wang *et al.*, Appl. Phys. Lett. **106**, 121104 (2015).

[54] M. Pavan *et al.*, Sol. Energy Mater. Sol. Cells **132**, 549 (2015).

[55] B. Kupfer, K. Majhi, D. A. Keller, Y. Bouhadana, S. Rühle, H. N. Barad, A. Y. Anderson, and A. Zaban, Adv. Energy Mater. **5**, 1401007 (2015).

[56] L. Wang, H. Ma, L. Chang, C. Ma, G. Yuan, J. Wang, and T. Wu, Small **13**, 1602355 (2017).

[57] D. Liu, S. Li, P. Zhang, Y. Wang, R. Zhang, H. Sarvari, F. Wang, J. Wu, Z. Wang, and Z. D. Chen, Nano Energy **31**, 462 (2017).

[58] F. Giordano, A. Abate, J. P. Correa Baena, M. Saliba, T. Matsui, S. H. Im, S. M. Zakeeruddin, M. K. Nazeeruddin, A. Hagfeldt, and M. Graetzel, Nat. Commun. **7**, 10379 (2016).

[59] Y. Yan, M. Li, X. Wang, W. Lu, and H. Shen, Mater. Lett. **253**, 156 (2019).